Experimental and computational characterisation of the effect of manufacturing-induced defects on high temperature, low-cycle fatigue for MarBN

O'Hara, E.M.[1,5], Phelan, B.[3], Osgerby, S.[4], Barrett, R.A.[1,2,5], Raghavendra, R.[2,3], Leen, S.B.[1,2,5], Harrison, N.M.[1,2,5]

[1]Mechanical Engineering, NUI Galway, University Road, Galway, Ireland.

[2] I-Form Advanced Manufacturing Research Centre, Ireland

[3]South Eastern Applied Materials Research Centre, Waterford Institute of Technology, Waterford, Ireland.

[4]GE Power, Newbold Road, Rugby, Warwickshire, United Kingdom

[5] Ryan Institute for Environmental, Marine and Energy Research, NUI Galway, Ireland

Abstract

Manufacturing-induced defects are a key source of crack initiation and component failure under high temperature cyclic loading. In this work, 3D X-ray micro-computed tomography and microstructural analysis of manufacturing-induced defects is presented for forged and cast MarBN martensitic-ferritic steel, along with high temperature, low cycle fatigue testing, for assessment of the comparative effects of two manufacturing processes. Forging is found to significantly reduce the volume fraction and complexity of manufacturing defects, compared to the cast material, and as a result, approximately double fatigue life. A voxel-based finite element methodology for experimentally-identified cast and forged manufacturing defects is presented, in conjunction with a multiaxial, critical-plane damage model, within a unified viscoplastic user-material subroutine. The effect of the complex morphologies of the manufacturing defects on high

temperature fatigue crack initiation is thus quantified, highlighting the relative effects of the two different manufacturing processes.

Keywords

Defects; Fatigue crack initiation; X-ray computed tomography; High-temperature deformation; Martensite.

Declaration of Interest – None.

1. Introduction

European energy production from renewables is increasing rapidly; however, due to the generally highly-variable nature of renewable energy, there is also an urgent need for fossil fuel power plant to operate highly flexibly and, ideally, at increased temperatures, to reduce harmful emissions [1]. Increased power plant cycling causes significant dynamic thermal and stress loading of components, leading to increased microstructural damage. Combined creep-fatigue loading has been identified as a major contributor to reduced component lifetime, increasing plant costs and outage rates [2]. The effect of high temperature creep loading on power plant materials has been extensively investigated, in line with the typical loading conditions a traditional base-load power plant component would encounter [3–6]; however, as plant infrastructure is re-tasked for higher temperature and flexible operation, new candidate materials may be required in critical components in order to meet the new in-service thermomechanical fatigue-creep requirements.

Nickel-based superalloys can provide many of the desired material properties for application at elevated loading conditions, but the significant cost associated with these materials means retro- or outfitting of an entire plant is not economically viable. Hence, substantial resources have been focused on the development of further modifications to 9Cr alloys for these applications [7]. In order to achieve desired mechanical properties under complex thermomechanical fatigue-creep loading within a high temperature oxidising environment, careful consideration of chemical composition during melting and refinement of these materials is required. Small variations in chemical composition can have adverse effects under ultra-supercritical (USC) loading conditions. Furthermore, trace elements, such as calcium, must be stringently controlled during deoxidisation of the steel. Secondary refinement is typically required for USC grade materials, for example via argon oxygen decarburisation or vacuum oxygen decarburisation. The fabrication of a highly homogeneous material, with uniform elemental distribution is a vital requirement in the production of a high quality steel for USC applications [7].

The presence of manufacturing defects (e.g. voids and inclusions) is a potential cause of reduced fatigue performance for high strength alloys. A number of factors including matrix material, inclusion type and interface properties can affect fatigue cracking behaviour [8]. Inclusions occur in metallic alloys as a result of chemical reactions with the environment during manufacture and substantial financial resources have been invested in reducing such discontinuities in steels. The presence of inclusions typically leads to void formation and premature cracking of components under in-service conditions. Increased plastic deformation and stress- and strain-localisation occur at the interfaces between inclusions and the matrix [9–14], with consequent direct effects on crack propagation, causing cracks to preferentially move towards an inclusion, for example. It is important to understand the effects of voids and inclusions under various high temperature fatigue loading conditions

via experimental and computational methods [14–18]. For example, Wang *et al.* [19] identified $CaO\text{-}Al_2O_3$ inclusions in a linepipe steel (X80), following the ladle furnace-degassing-Ca treatment stage of manufacture. Modifications to the manufacturing process were investigated and an inclusion removal step was found to reduce the number of inclusions by over 40%, as well as reducing their size.

Modelling of idealised (i.e. spherical) defect geometries has been performed by multiple authors [16,18,20,21] to identify the localised effects of such discontinuities on the matrix and fatigue crack initiation (FCI). This has provided insight into the primary micro-scale mechanisms of degradation occurring, specifically the influence of the localised stress-strain field on matrix-inclusion decohesion, as well as strain accumulation (ratchetting) and the importance of defect shape, size and location. In contrast, the computational modelling of realistic, complex defects has received relatively little attention, despite the obvious importance of void or inclusion morphology on local stress and strain concentrations [17,22–24].

This paper presents a combined experimental and computational investigation of the influence of manufacturing-induced defects in cast and forged MarBN, a tempered martensitic steel, for application in next generation power plants. High temperature low cycle fatigue (HTLCF) testing is performed to investigate the fatigue response of cast and forged MarBN, with comparison to rolled P91, a widely used material in current generation (subcritical) power plants. Microstructural analysis of post-test MarBN is performed, with a view to understanding the effects of the manufacturing process and defects on FCI and component failure at high temperature. 3D X-ray micro-computed tomography (μCT) scanning of cast and forged MarBN, before and after HTLCF testing, is performed to better understand the influence of manufacturing process on defect formation

and associated FCI, via identification of defect volume fraction and shape characterisation, including analysis of the primary crack path, and micro-cracking between defects. A voxel-based finite element methodology is developed to represent the complex morphology of the measured defects for both manufacturing processes. A multiaxial, critical-plane Ostegren model for thermo-mechanical fatigue damage is implemented within a hyperbolic sine unified viscoplasticity model, with combined non-linear kinematic-isotropic hardening-softening. It has thus been possible to computationally characterise the effects of the complex morphologies of manufacturing defects on the HTLCF performance of MarBN, with specific focus on localised strain, fatigue damage and crack initiation.

2. Methodology

2.1. High Temperature Low Cycle Fatigue Testing

The chemical composition and heat treatment for cast and forged MarBN presented here was developed as part of the IMPACT consortium project [25]. The typical chemical compositions of the MarBN steel (a new 9Cr steel with up to 3 wt.% W and Co, with controlled levels of B and N) studied in this work and more conventional P91 steel are compared in Table 1. Chromium is known to enhance oxidation and corrosion resistance at high temperature through the formation of a protective chromium oxide scale on the surface of components, as well as contributing to enhanced creep strength via formation of Cr rich $M_{23}C_6$ carbides following tempering. Tungsten and molybdenum also contribute to the strength of the material through solid solution strengthening. Vanadium and niobium combine with carbon and nitrogen to form MX carbonitrides, dispersed throughout the laths to resist dislocation motion. Boron and nitrogen content is strictly controlled, to prevent BN particle formation during heat treatment. Boron reduces the minimum creep

rate and provides enhanced stabilisation of carbides along boundaries, preventing lath coarsening for longer periods of time. Nitrogen also contributes to improving the long-term creep strength and cobalt has been found to inhibit delta ferrite formation and enhance material toughness [4–7].

Table 1. Chemical composition of P91 [26] and MarBN [27] steels in wt.%. The balance is made-up of Fe.

	Al	B	C	Co	Cr	Mn	N	Nb	P	Si	V	W
P91	0.007	-	0.12	-	8.60	-	0.060	0.07	0.017	0.34	0.24	0.03
MarBN (min)	-	0.005	0.074	2.91	8.77	0.48	0.001*	0.046	-	0.3	0.18	2.85
MarBN (max)	-	0.018	0.081	3.1	9.08	0.51	0.065*	0.055	-	0.31	0.2	3.13

The heat treatment for cast MarBN, undertaken at NUI Galway, is similar to the process described by Li et al. [28], to ensure BN formation does not occur. Figure 1 shows a schematic comparison of the heat treatment protocol for cast MarBN to that of conventional rolled P91 steel; the specific temperatures have been normalised due to commercial sensitivity. Normalisation is performed to increase the yield and tensile strength of the material in the 850 °C to 1250 °C temperature range. Upon rapid cooling following removal from the furnace, austenite-to-martensite transformation occurs as the material air cools below the martensite start temperature (approximately 380 °C for 9Cr steels). The hierarchical microstructure of martensite is key to the enhanced creep performance of 9Cr steel via the various micro-strengthening mechanisms [7]. Once the steel has cooled to room temperature, tempering is performed, at a lower temperature than

normalizing, to increase toughness, improve ductility and to form a precipitate strengthened tempered martensitic microstructure. This also reduces the dislocation density of the material and allows precipitation of $M_{23}C_6$ carbides and MX carbonitrides, which are essential to the long-term creep strength and grain boundary stability of the material [7].

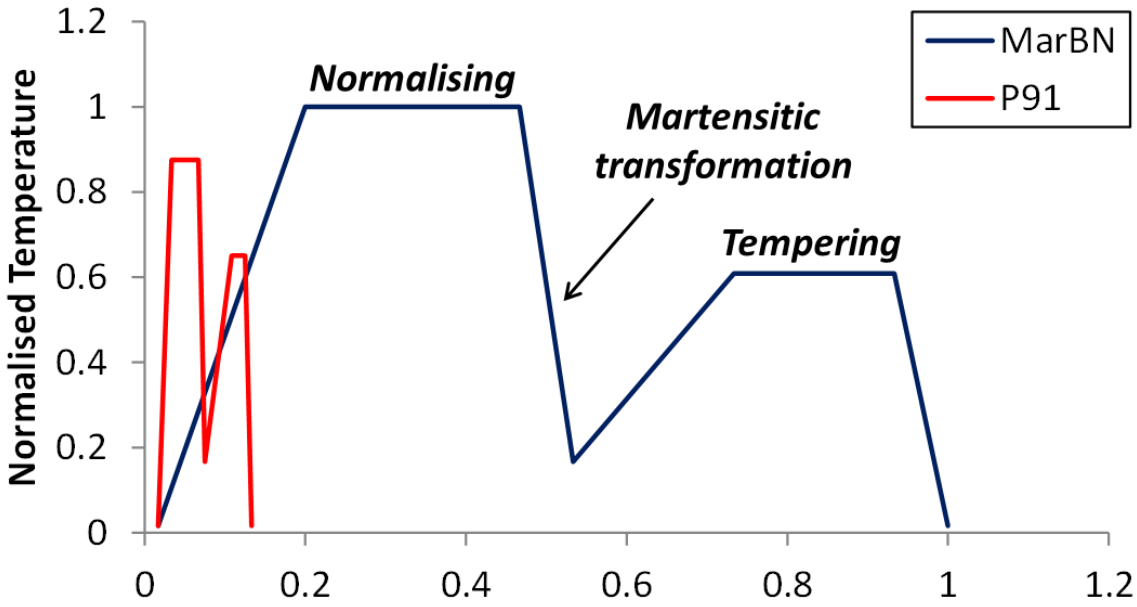

Figure 1. Comparison of heat treatment protocols for MarBN and conventional P91 steel.

Cylindrical specimen blanks were extracted from a cast plate and heat treatment was performed using a UAF 14/10 Lenton high temperature oven for normalization, followed by an AWF 130/12 Lenton high temperature oven for tempering. Forged MarBN, manufactured from the same cast plate, was received in heat treated condition (shorter than the cast). HTLCF cylindrical dog-bone specimens were then machined from the bars, according to ASTM E606 – 04 for strain-controlled fatigue testing. Casting allows manufacture of large, complex geometries, generally at a reduced tooling cost compared to forged components; in contrast, forging produces a more refined grain structure, with increased material toughness and reduced porosity [29]. Therefore, forged material

generally gives superior fatigue performance due to reduced grain size, compared to cast material. Strain-controlled HTLCF testing is performed using an INSTRON 8500 in conjunction with an INSTRON 8800 controller, at NUI Galway (T = 600 °C; strain-rate, $\dot{\varepsilon}$ = 0.1 %/s; total strain-range, $\Delta\varepsilon$ = ±0.5%). The failure criterion is defined as a 20% drop in load after the first 150 cycles of testing. Thermal calibration of the oven was previously performed for MarBN up to 700 °C at NUI Galway using high temperature thermocouples [30]. A more detailed description of HTLCF and creep-fatigue (CF) testing for the present cast MarBN has previously been presented for both 600 °C [31,32] and 650 °C [33]; the latter also provides details on calibration and validation of material parameters for unified cyclic viscoplastic modelling described below.

2.2. Microstructural Analysis

Samples are cut from (i) as-received heat-treated bars and (ii) the gauge length of post-HTLCF test MarBN samples using a Buehler IsoMet low speed saw for analysis using scanning electron microscopy (SEM) and transmission electron microscopy (TEM). For SEM, samples are mounted and polished using a Buehler EcoMet/AutoMet 250 Pro automatic polisher to a 0.06 µm finish, followed by etching with Vilella's reagent.

Carbon replica and twin jet polishing preparation techniques were used for TEM analysis. Carbon replica sample preparation is the same as that of SEM, followed by application of a continuous carbon layer using a vacuum carbon evaporator. A 2 mm^2 grid is cut on the sample surface and placed in Vilella's reagent until the carbon layer detaches from the sample. Each section is placed on a copper mesh grid for analysis. TEM of carbon replica and thin foil samples is performed using a Hitachi H7000 TEM at NUI Galway and a JOEL JEM-2100F TEM at University of Limerick.

For twin jet polishing, a thin section of metal is cut using a slow speed saw and gradually ground to between 50 µm and 100 µm thickness, with a P4000 grit finish. A disc punch is used to extract 3 mm discs from the larger sample. Samples are then placed in the twin jet polisher, containing a methanol-based etchant (methanol – 59 %, perchloric acid – 6 %, buchanol – 35 %), at -27 °C and a voltage of 20.5 V. Etchant is fired at the disc from both sides to produce a hole, with a surrounding area thickness of approximately 200 nm.

2.3. 3D X-Ray Micro-Computed Tomography

3D X-ray µCT scanning of one cast and one forged MarBN sample (20 mm in length and 6.5 mm diameter) is performed at the South Eastern Applied Materials (SEAM) research centre at Waterford Institute of Technology, before and after HTLCF testing, using a GE VTOMEX L300. The scans are completed at a voltage of 230 kV, a current of 65 µA and integration timing of 250 ms. The source used is a 300 kV open X-ray source provided by GE, which gives a 14.95 µm focal spot onto a tungsten target. Six integrations are averaged to create a single image and two skip frames are used between movements over a total of 1,800 integrations during which the sample is rotated through 360°. The focus-detector-distance is 840 mm and the focus-object-distance is 42 mm. In combination with a GE DXR250 digital detector array, a 400 x 400 mm panel with 2000 x 2000 pixels is used, which yields a geometric magnification factor of 20 and a voxel size of 10 µm.

The Feldkamp region, defined as a region of artefacts due to transversal penetration of the sample near the outer region of the X-ray cone beam [34], is excluded from analysis; therefore, 18 mm and 16 mm of the centre sections are used for 3D reconstruction using Materialise Mimics 18.0 and Materialise 3-Matic 10.0 for cast and forged MarBN, respectively. Two key types of defects identified are inclusions and voids, based on the significant difference in density compared to the matrix material. A filter is applied in 3-

Matic to remove noise and image-based artefacts in the samples. The increased volume fraction of defects identified in the cast sample, compared to the forged, leads to increased noise and therefore, a higher filter threshold is applied.

2.4. Material Model

As previously presented by the authors [32], MarBN displays a complex cyclic non-linear softening behaviour under HTLCF testing conditions. A unified cyclic viscoplasticity model, incorporating combined non-linear kinematic hardening and isotropic softening, implemented using an implicit solver within a user-material subroutine, is therefore adopted here. Furthermore, in order to computationally characterise the expected detrimental effects of complex-morphology defects on fatigue damage using three-dimensional modelling, a new multiaxial, critical-plane life prediction methodology is incorporated here within the latter user-material subroutine. Previous work by the authors examined the effects of idealised spherical manufacturing defects [33]. However, in this paper, attention is focussed on the key role of the complex geometry of manufacturing defects, as measured experimentally.

The plastic strain-rate tensor, $\dot{\boldsymbol{\varepsilon}}^{\mathrm{pl}}$, is defined as follows:

$$\dot{\boldsymbol{\varepsilon}}^{\mathrm{pl}} = \frac{3}{2}\alpha \sinh\beta\left(\mathrm{J}_2\left(\tilde{\boldsymbol{\sigma}}-\boldsymbol{\chi}\right)-R-k\right)\frac{\tilde{\boldsymbol{\sigma}}-\boldsymbol{\chi}}{\sigma_{\mathrm{e}}} \tag{1}$$

where α and β are viscoplastic material parameters, $\tilde{\boldsymbol{\sigma}}=\dfrac{\boldsymbol{\sigma}}{\left(1-D\right)}$ is the damaged stress tensor, D is fatigue damage, $\boldsymbol{\chi}$ is the Armstrong-Frederick [35] kinematic back-stress tensor, R is the Chaboche [36] isotropic softening stress, k is the initial cyclic yield stress, and σ_{e} is von Mises equivalent stress. Damage accumulation is calculated at the

end of each cycle, based on the current prediction for cycles to crack initiation, using the following Chaboche [37] equation:

$$D = 1 - \left[1 - \left(\frac{N}{N_{\mathrm{i}}(N)} \right)^{\frac{1}{1-\phi_1}} \right]^{\frac{1}{\phi_2 - 1}} \tag{2}$$

where ϕ_1 and ϕ_2 are material constants. The Ostergren [38] model is adopted for prediction of number of cycles to crack initiation as follows:

$$N_{\mathrm{i}}(N) = C \left[\max_{\mathrm{n}} \left(\Delta\varepsilon_{\mathrm{n}}^{\mathrm{pl}}(N) \sigma_{\mathrm{max,n}}(N) \right) \right]^{\delta} \tag{3}$$

where N is the current cycle number, C and δ are material parameters, and the maximum stress, $\sigma_{\mathrm{max,n}}$, and plastic strain-range, $\Delta\varepsilon_{\mathrm{n}}^{\mathrm{pl}}$, are identified with respect to plane orientation, n, from 0° to 180° in increments of 10° [39].

2.5. Computational Modelling

A key challenge of the present work is to computationally represent the multi-axial cyclic viscoplastic evolution of the stress, strain and fatigue damage distributions associated with complex-morphology defects in three-dimensional models. In this context, representation of the entire gauge length with associated measured distribution of defects is not generally feasible, particularly considering the need for highly refined meshes in the critical localisation regions around defects. As a result, a new methodology is presented here to develop voxel-type models of the measured cast and forged manufacturing-induced defects in the HTLCF samples.

Figure 2 describes the process used for 3D model development of the cast and forged HTLCF gauge length models. Reconstruction of dicom files, in terms of manufacturing defects, is performed using Materialise Mimics 18.0 and Materialise 3-Matic 10.0. An STL file of each respective sample is created and exported to Autodesk Netfabb where each individual defect is quantified in terms of length, area and volume. The largest defects are segregated and exported as an STL file. In Abaqus, this file is overlaid on a solid model of the HTLCF gauge length. Hexahedral meshing of the solid cylinder, to an element size of 40 μm (due to computational limitations) is performed, and an input file is generated. A custom written MATLAB code, implementing the nearest neighbour algorithm, is written to identify overlapping regions between the solid cylinder model and defects. This data is written to an input file, in the form of voxel-type defects, and converted to an STL file. In Autodesk Netfabb, Boolean subtraction of the voxel-type defects from the cylinder is performed and tetrahedral re-meshing of the cylinder (containing defects) is performed in NetGen to increase element size in regions away from the defects while maintaining overall geometric accuracy and element quality, as verified within Abaqus. Although the use of voxels results in a small sacrifice in terms of defect shape, the final model benefits in terms of high-quality finite element meshing, free from both warnings and errors, with significantly reduced runtime and computational expense.

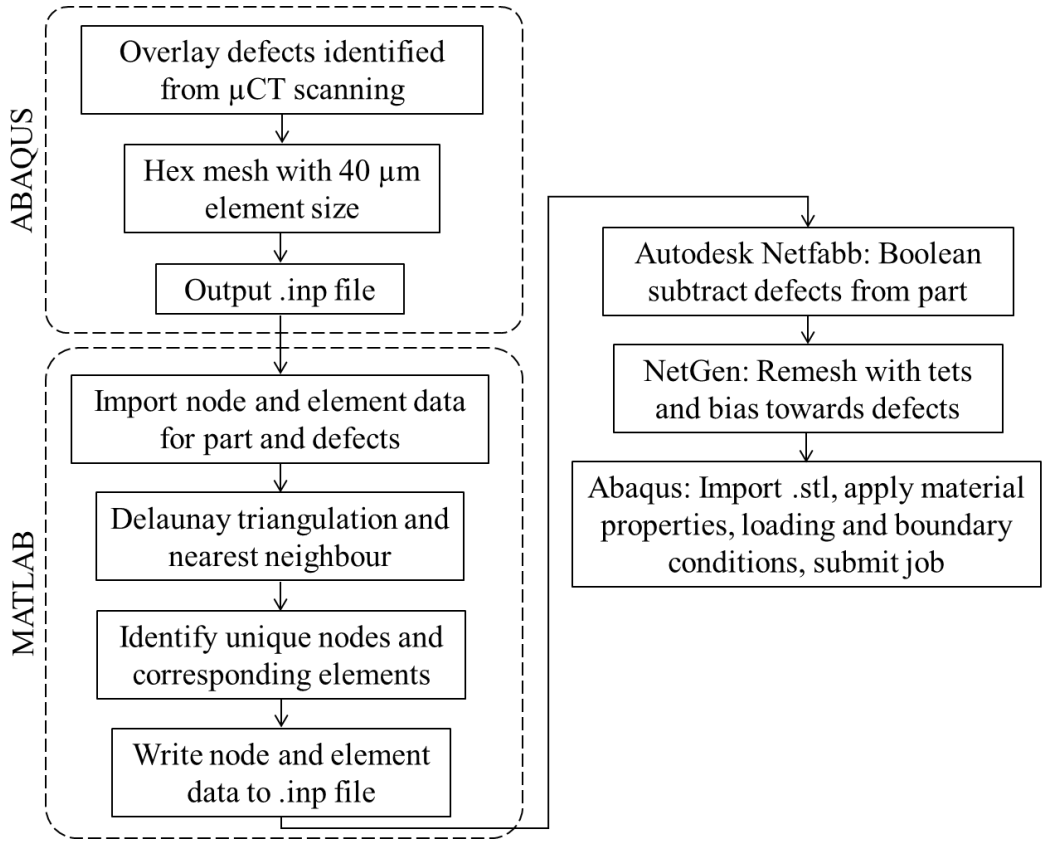

Figure 2. Flowchart for creation of the voxel-type defect geometry.

The above voxel-based methodology allows for significant reduction in the number of elements in each model, compared to an original hexahedral mesh (between 91% and 98% in all cases). Four-node tetrahedral elements (C3D4) are used following re-meshing.

Figure 3 illustrates the boundary conditions applied to the cast and forged HTLCF gauge length. Material properties for cast MarBN at 600 °C [32], and HTLCF loading and boundary conditions (strain-rate, $\dot{\varepsilon}$ = 0.1 %/s and total strain-range, $\Delta\varepsilon$ = $\pm$0.5%) are applied, as per the loading conditions experienced by the μCT scanned samples.

It has been previously shown by O'Hara [40], in a study which explicitly compared spherical-shaped voids and inclusions, that the stress and strain localisations (and related fatigue lives) associated with voids and inclusions were very similar. In the latter work, the inclusion-matrix contact was explicitly modelled, along with cohesive zone modelling of

decohesion. The additional modelling complexity for the inclusions is therefore apparently not justified. Consequently, it is considered reasonable, in the context of assessment of the mechanical effects of fatigue damage due to cyclic stress-strain localisation here, to represent all measured defects as voids, i.e. no explicit representation of inclusion-matrix contact and decohesion.

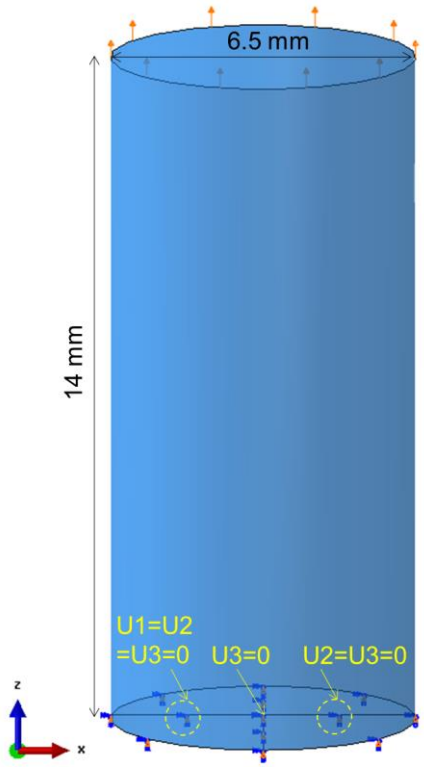

Figure 3. Loading and boundary conditions applied to the HTLCF gauge length.

3. Results

3.1. Experimental Testing

In Figure 4, a direct comparison of the HTLCF behaviour between cast and forged MarBN and rolled P91 steel is shown. Figure 4(a) presents the stress-strain data at the initial and half-life cycles for all samples. The yield stress of one of the cast samples (~250 MPa) is found to be approximately 25% lower than the second cast sample and both forged samples (~330 MPa). In Figure 4(b), cycles to failure for a single rolled P91 sample, and

the average life for two cast and forged MarBN samples are presented, including error bars of standard deviation. In Figure 4(c), significant differences in prior austenite grain (PAG) size can be observed for the different manufacturing processes. Rolled P91 has a refined PAG size of approximately 20 µm; the cast MarBN has a greater variation in PAG size in the range of 200 µm to 400 µm; the forged MarBN has an intermediate PAG size of approximately 100 µm in length, as measured by optical microscopy.

Figure 5 presents TEM images of cast MarBN in the as-received (Figure 5(a)) and post-test (Figure 5(b – d)) condition. $M_{23}C_6$ carbides distributed along lath boundaries are identified in the as-received material. Low angle boundary annihilation and subgrain formation is observed as a result of HTLCF loading.

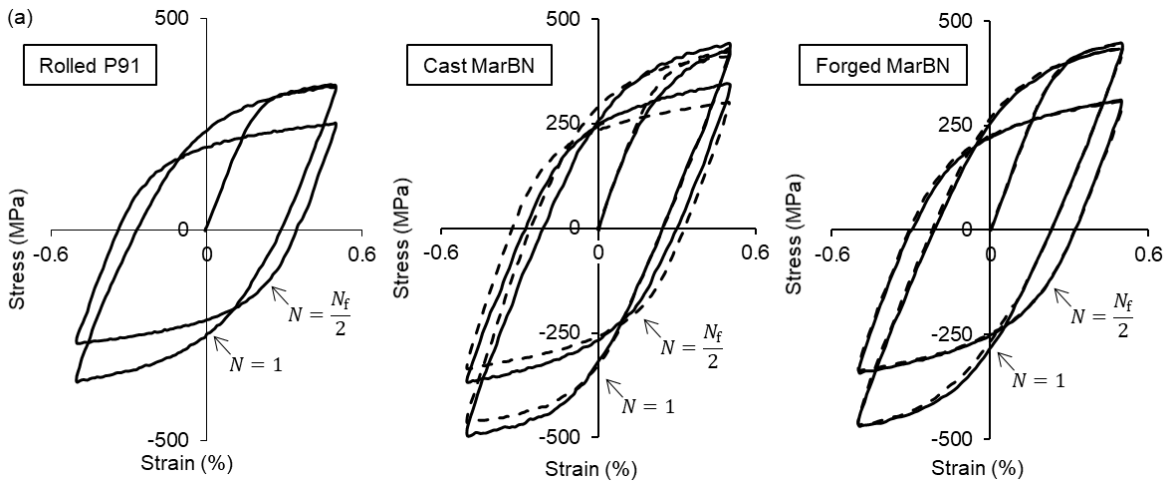

297

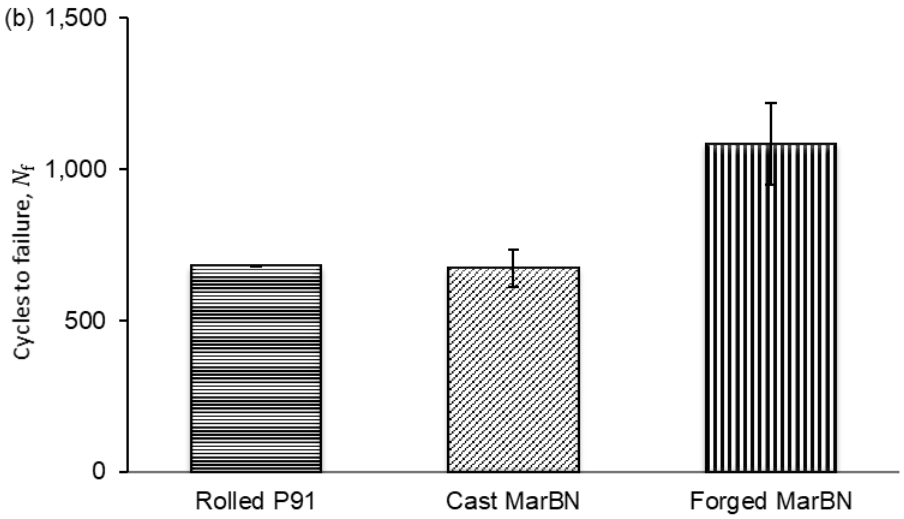

298

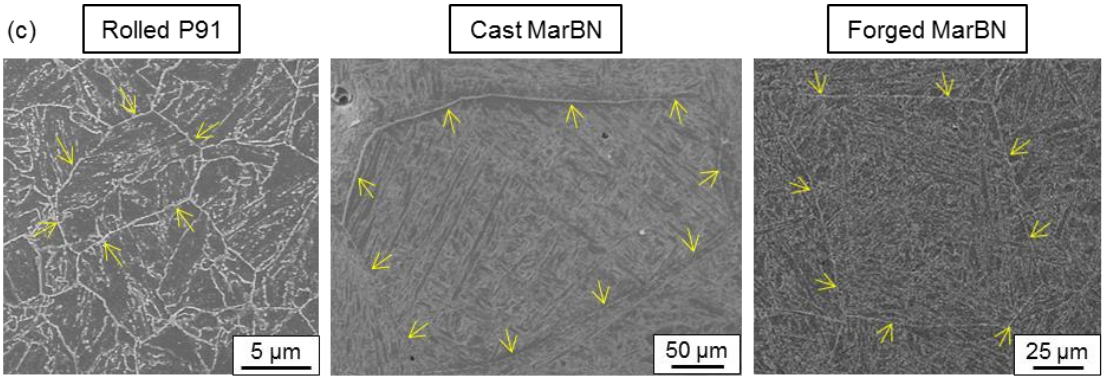

299 Figure 4. (a) Initial and half-life stress-strain loops, (b) cycles to failure, and (c) scanning
300 electron microscope images of the grain structure of rolled P91 (T = 600 °C, n = 1), cast
301 MarBN and forged MarBN (T = 600 °C, n = 2). $\dot{\varepsilon}$ = 0.1 %/s and $\Delta\varepsilon$ = ±0.5%. Yellow
302 arrows denote the grain boundary.

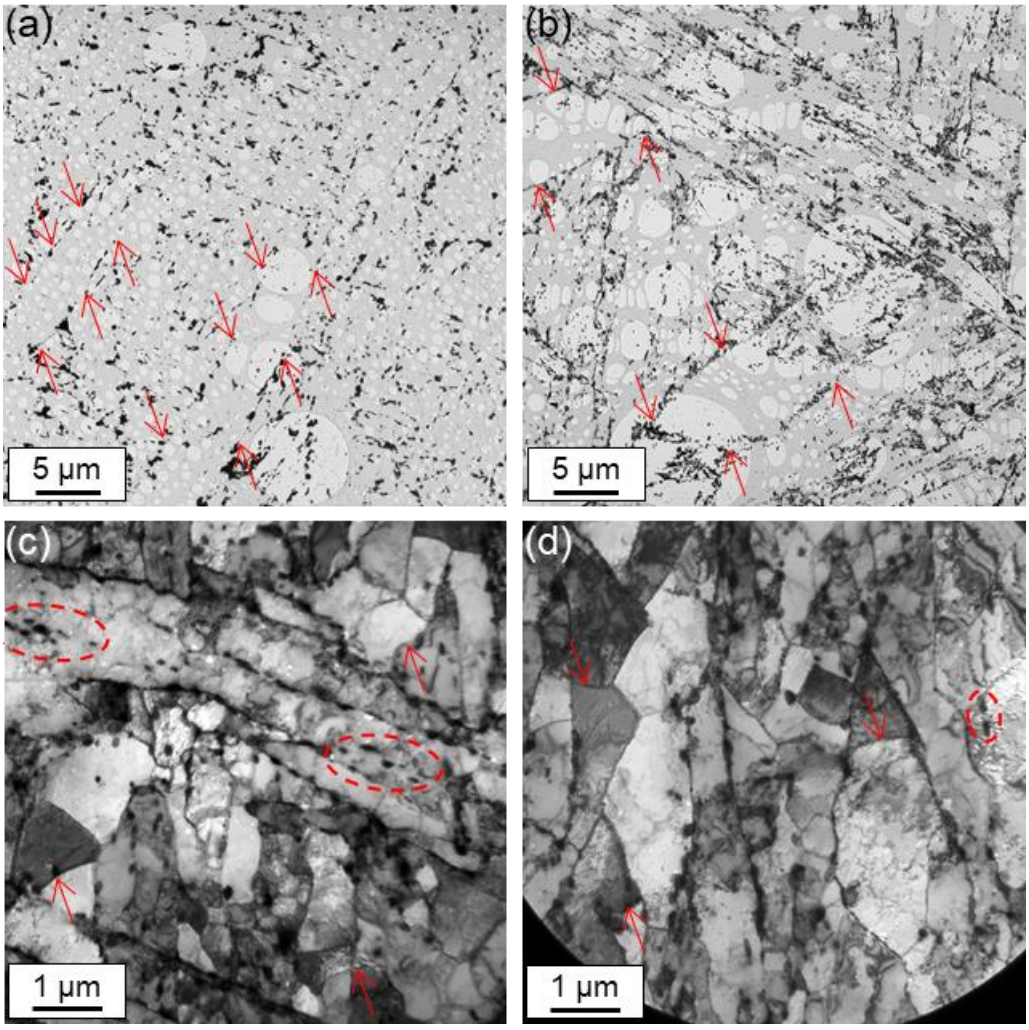

Figure 5. Transmission electron microscopy images of carbon replica (a, b) and thin foil (c, d) cast MarBN samples in the (a) as-received and (b, c, d) post-test condition. Red arrows highlight lath or subgrain boundaries, and dashed circles highlight $M_{23}C_6$ carbides.

3.2. 3D X-Ray µCT Scanning

Figure 6 shows the 3D reconstruction of manufacturing defects in the cast (blue) and forged (red) MarBN samples for both pre-test (Figure 6(a, b)) and post-test (Figure 6(c, d)) from the top and side views, respectively. The volume fraction of manufacturing defects in the as-received material has been identified, via reconstruction of 3D X-ray µCT scanned HTLCF samples, as 0.03% and 0.002% for cast and forged MarBN, respectively. A large crack is clearly visible in the post-test cast sample, as a result of HTLCF loading at 600 °C

(Figure 6(c)). Stringer type defects [19], elongated in the direction of forging, are identified in the forged sample, as distinct from the complex shapes in the cast material. Multiple cracks are also found to occur in the forged sample along the majority of the circumference (Figure 6(d)), compared to a single large crack in the cast. Figure 7 shows a comparison of a post-test forged manufacturing defect imaged using SEM, with the same geometry reconstructed via 3D X-ray µCT scanning.

In Figure 8(a), the crack in the cast sample is isolated, with embedded defects highlighted as causes of crack initiation and propagation. Figure 8(b) presents two cracks in the forged sample at stringer-type manufacturing defects. Figure 9(a) shows examples of the complex shaped casting defects observed in the as-received (blue) and post-test (red) cast condition. Many of the defects are shown to be elongated with multiple branches, and holes appear to be prime locations for void growth as a result of HTLCF testing. In contrast, Figure 9(b) highlights some examples of coalescence of stringer-type defects in the forged MarBN sample following high temperature cyclic loading. To quantitatively compare the defects identified in the cast and forged MarBN samples, sphericity, S, is used. This is the ratio of the surface area of a sphere with the equivalent volume as the defect (A_{eq}), to the surface area of the defect (A_{defect}) and is plotted against the effective radius of the sphere, where S = 1 is a perfect sphere [41]. This methodology has been applied previously for characterisation of casting defects in Al-alloys [24] and creep cavity formation in 9Cr steels [42]. Sphericity has been applied here to each individual manufacturing defect identified in the pre-test cast and forged MarBN samples. Figure 9(c) compares effective radius (of a sphere with an equivalent volume) versus sphericity for the ten largest cast and forged defect volumes. The sphericity of cast defects is generally lower, as per the

increased complexity of larger cast defects, with a typically increased effective radius, compared to the forged defects.

In Figure 10, SEM images of the influence of manufacturing defects on crack initiation and propagation behaviour on the fracture surface of cast (a, b) and forged (c, d) MarBN are presented. Backscatter electron (BSE) microscopy images of secondary cracking along the gauge length of cast (e, f) and forged (g, h) MarBN samples indicate that manufacturing defects close to the surface are influential in crack initiation and propagation behaviour. Oxide scale growth in secondary cracks and oxide pitting at defects is identified in both samples.

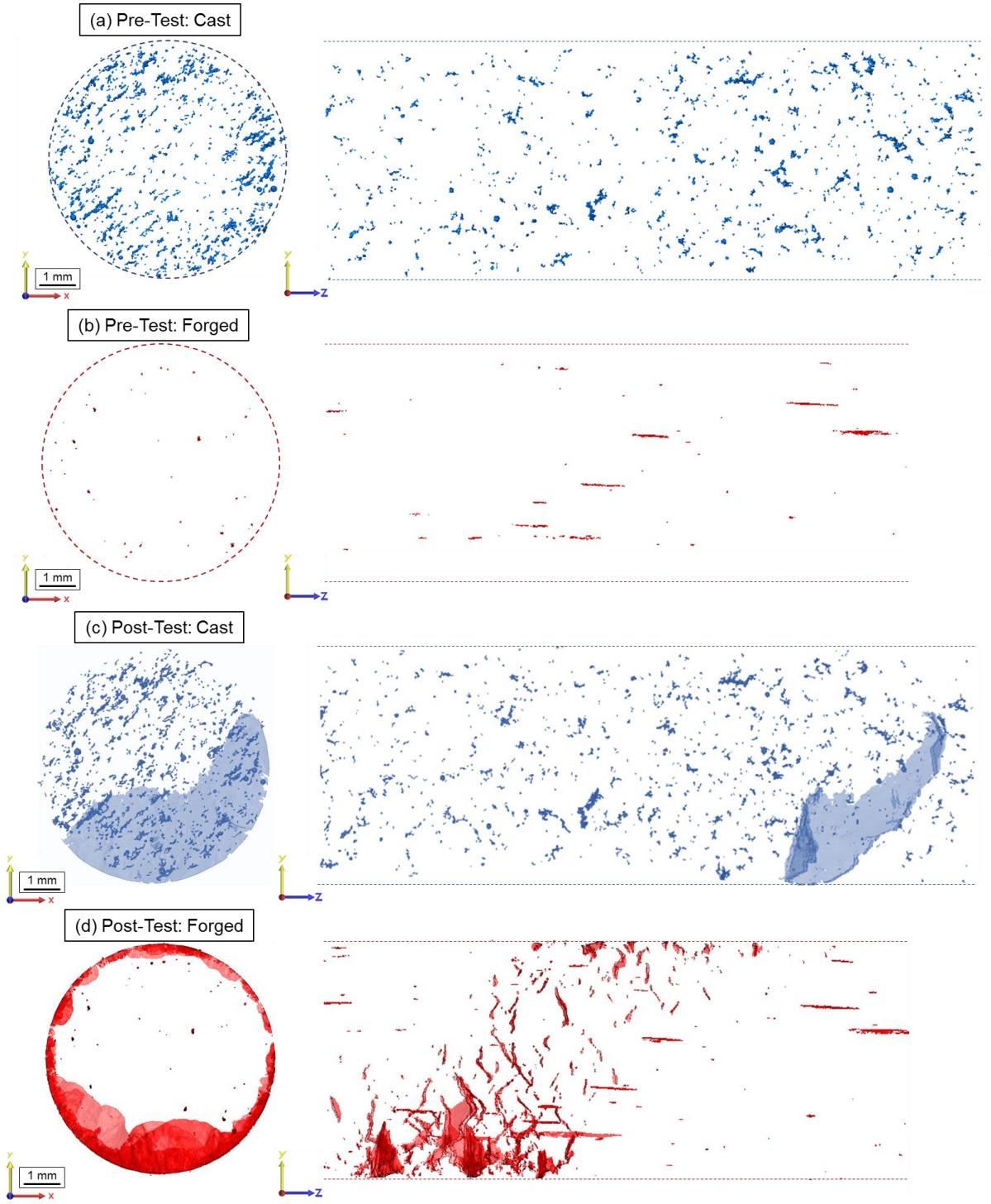

Figure 6. Reconstructed 3D X-ray µCT scans of cast and forged MarBN (a, b) before and (c, d) after high temperature low cycle fatigue testing at 600 °C, $\dot{\varepsilon}$ = 0.1 %/s and $\Delta\varepsilon$ = ±0.5%.

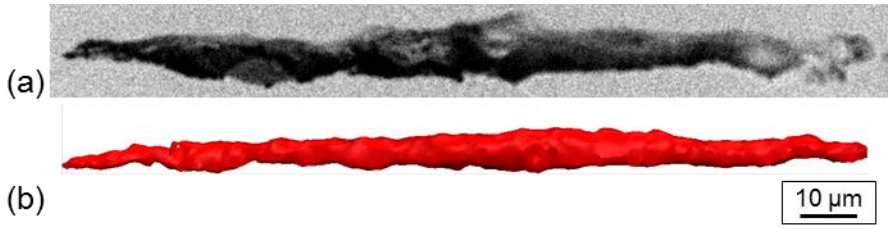

350

351 Figure 7. Comparison of a post-test forged manufacturing defect identified via (a) SEM

352 and (b) 3D X-ray µCT scanning.

353

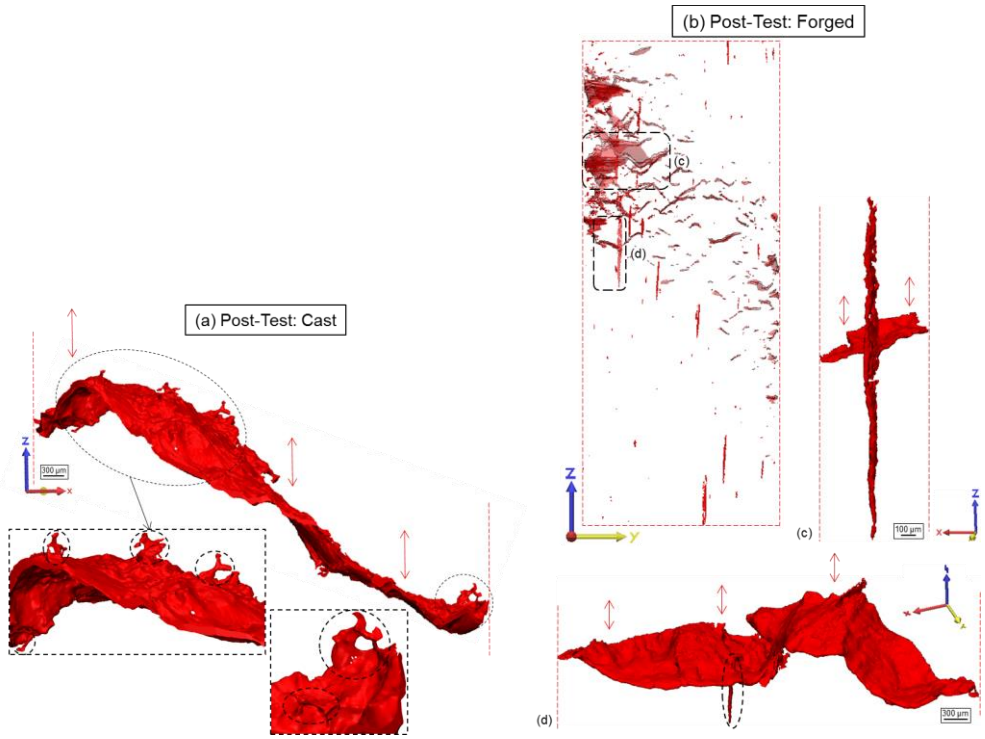

354

355 Figure 8. Identification of manufacturing defects in regions of cracking in the (a) cast and

356 (b) forged MarBN samples after HTLCF testing. Dashed circles highlight defects.

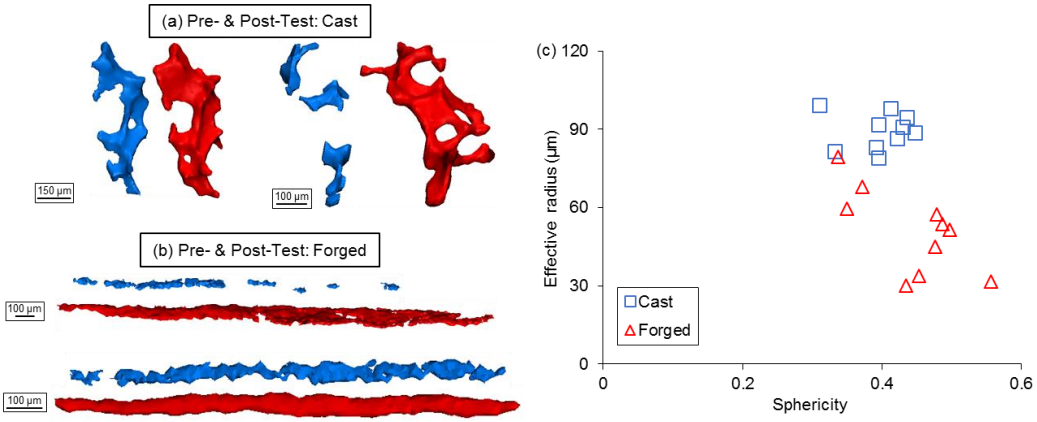

357

358 Figure 9. Comparison of various manufacturing defects in (a) cast and (b) forged MarBN
359 before (blue) and after (red) HTLCF testing. (c) Effective radius versus sphericity for the
360 ten largest pre-test cast and forged defect volumes.

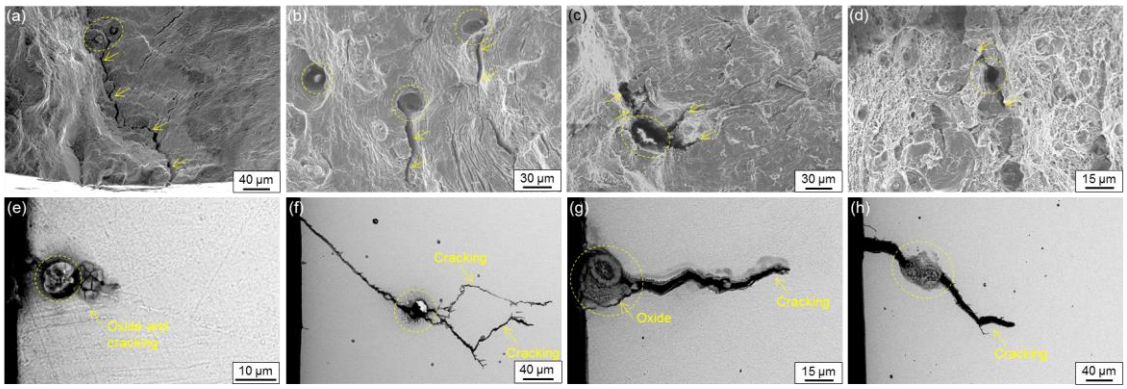

361

362 Figure 10. Manufacturing defects (dashed circles) and cracking (arrows) on the fracture
363 surface of (a, b) cast and (c, d) forged MarBN post-HTLCF testing. Gauge length cracking
364 in the region of manufacturing defects (dashed circles) and oxide pit formation in (e, f)
365 cast and (g, h) forged MarBN post-HTLCF testing.

366 ### 3.3. Computational Modelling

367 In Figure 11, the largest defects identified during µCT scanning are compared to the
368 resulting Abaqus model for the cast and forged conditions, as per the method of Section
369 2.5.

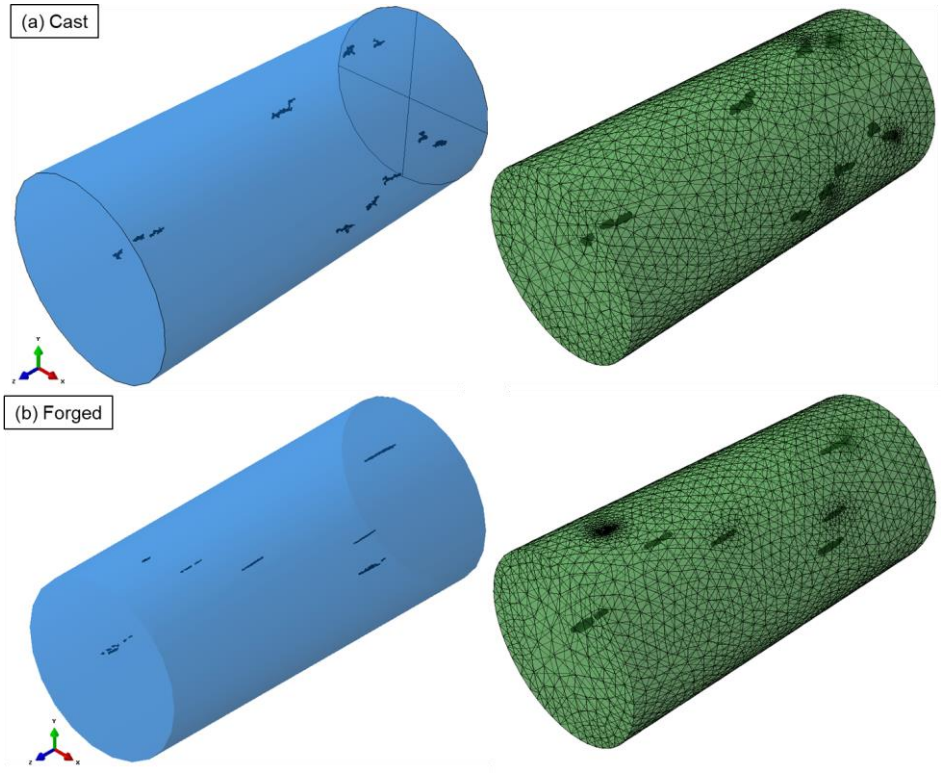

Figure 11. Comparison of the largest defects identified from µCT scanning (left) and Abaqus model (right) for (a) cast and (b) forged geometries.

Figure 12 presents iso-surface plots of maximum principal strain (a, b) and damage (c) distributions, localised in the region of cast and forged defects, after two cycles. The strain concentration factor (SNCF), based on maximum principal strain, is ~11 and ~3 for the cast and forged models, respectively, increasing the likelihood of crack initiation in the region of defects. For the cast MarBN material, propagation of the strain iso-surfaces across ligaments between defects is also observed, when defects are closely located. The predicted maximum value of damage in the cast model (~0.27) is four orders of magnitude higher than that of the forged (~0.00009).

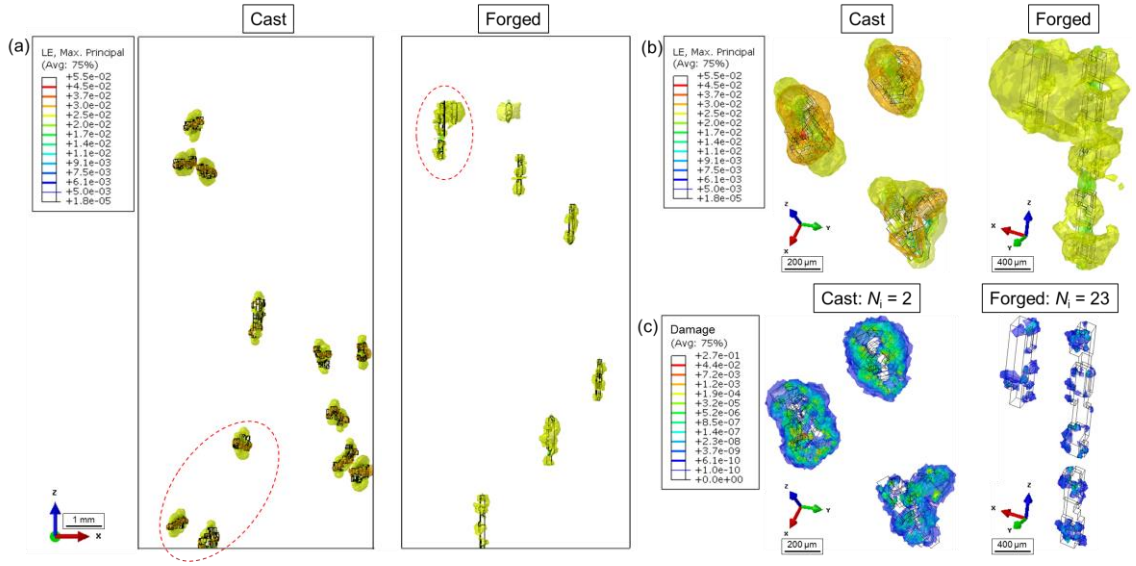

Figure 12. (a) Maximum principal strain iso-surface distributions in the cast (left) and forged (right) HTLCF gauge length models. (b) Maximum principal strain and (c) damage iso-surfaces, highlighted by the dashed circles in part (a).

4. Discussion

The cast MarBN material shows comparable performance to the rolled P91, with superior cyclic strength (Figure 4(a)) at the initial (up to 28.5%) and half-life (up to 34.4%) cycles, and equivalent fatigue life (Figure 4(b)). This is attributed to (i) improved solid solution strengthening via W solute atoms and (ii) a more refined low-angle boundary microstructure, resulting from a finer distribution of $M_{23}C_6$ carbides as tungsten content increases [43]. The stress range of the forged material is similar to that of cast MarBN; however, the fatigue life is significantly increased, by a factor of approximately 2, indicating the key influence of manufacturing process on fatigue life. The stress-strain loops of cast and forged MarBN indicate greater differences in the behaviour of the two cast samples tested, but no significant difference overall in terms of cyclic strength or plastic strain-range. The similar constitutive behaviour for forged and cast MarBN, as presented in Figure 4, also indicates the key role of strengthening mechanisms such as

laths, precipitates and solid solution strengthening (Figure 5), with prior austenite grain size providing minimal contribution to yield strength and constitutive behaviour at 600 °C based on the large variation of grain size between cast (~300 μm) and forged (~100 μm) MarBN.

Cyclic softening, a well-known phenomenon for 9-12Cr steels attributed to dynamic recovery of the microstructure, is observed for all three materials tested. This dynamic recovery is consistent with a reduction in dislocation density, dominated by low angle boundary dislocation annihilation, resulting in lath coarsening (as observed in Figure 5(b – d)), the extent to which depends on temperature and strain amplitude. Therefore, even small-amplitude cycling of plant components (e.g. warm starts, hot starts or fluctuations) may cause microstructural degradation and reduce strength [44–46].

The initial PAG size in cast MarBN is shown to be many times larger than for rolled P91. Forging, in conjunction with a shorter heat treatment, results in a reduced PAG size compared to cast MarBN (~two to four times), cf. Figure 4(c). Thus, the high initial yield strength of MarBN, prior to cyclic softening, has been attributed to thermally stable, boron-enriched $M_{23}C_6$ carbides along boundaries (Figure 5), providing barriers to dislocation motion, combined with enhanced tungsten solid solution strengthening and high dislocation density [27,33,47,48]. This is a key benefit of MarBN for application to higher temperatures and pressures, compared to current materials in steam header applications, and is particularly encouraging in terms of the potential for a rolled MarBN equivalent.

Maruyama *et al.* [49] have shown that tungsten also reduces the coarsening rate of $M_{23}C_6$ carbides, enhancing the effect of precipitate strengthening. Previous analysis of $M_{23}C_6$ carbide growth by O'Hara *et al.* [33] indicated no significant change in carbide diameter as

a result of HTLCF loading. However, the number of particles was found to almost triple. Using BSE, this has been attributed to tungsten rich Laves phase (Fe_2W) formation [40], which are prone to rapid coarsening in-service [50]. In P92 steel, these particles have been identified as significant contributors to precipitate strengthening, as particles reach a similar saturated size to $M_{23}C_6$ carbides in less than 10,000 hours and contribute to precipitate strengthening along boundaries [51,52]. The saturated particle size of Fe_2W in cast MarBN is a potentially interesting focus for future work on the long-term effect of Laves phase formation and growth under flexible loading.

The manufacturing process plays a significant role in both the volume fraction and geometries of defects in cast and forged MarBN, as shown in Figure 6. The forged material is manufactured from the same melt as the cast sample scanned here. Therefore, both materials started out with similar defect characteristics. The forging process has a dramatic effect on defect geometry and distribution. The complex-shaped casting defects, with a volume fraction of 0.03%, are replaced by stringer-type geometries, with a volume fraction of 0.002%, aligned in the direction of forging (Figure 6 and Figure 9), thus indicating apparent consolidation of voids and defects, with reduction of volume fraction, leading to a significant increase in fatigue life. There is also less variability in measured stress-strain hysteresis loops for the forged sample compared to the cast (see Figure 4(a)), presumably attributable to the reduced volume fraction and complexity of defects.

This study did not examine the effect of orientation on the stringer defects in the forged sample, in relation to the direction of loading. However, fully-reversed fatigue testing of bainitic steel has previously indicated reduction in average fatigue limit of ~13% for samples taken perpendicular to the rolling direction [53].

The cracking behaviour is noticeably different between samples, whereby the cast sample has one large dominant crack. In contrast, the forged sample has multiple smaller cracks, distributed around almost the entirety of the circumference. Comparing Figure 6(a) and (c), the density of defects is greater in the region where fatigue cracking occurs, and void growth around defects can also be seen as a result of HTLCF loading. Similar coalescence of complex cavities has been identified in an Al-alloy for superplastic forming applications using μCT methods, and the rate of growth of cavitation volume was found to increase exponentially as the strain level is increased [54].

Defect geometry in the cast sample is highly complex (Figure 9(a)), comprising of multiple branches, and the influence of these discontinuities is clearly identified in Figure 8(a), where multiple complex-shaped defects are identified as part of the primary crack. Isaac *et al.* [55,56] have used X-ray computed tomography methods to quantify the volume change of creep cavities in a brass alloy, with void growth occurring below 25% of time to rupture, particularly at complex shaped defects. Although this paper presents results for samples in the as-received condition and after HTLCF testing, it is assumed that micro-cracking at defects occurs in the primary stages of loading, leading to propagation and coalescence during the remainder of testing [57].

The cast and forged defects with the ten largest volumes have been isolated (Figure 9(c) and Figure 11). In general, the largest casting defects are found to have an (i) increased effective radius and (ii) reduced sphericity, compared to the largest defects in forged MarBN. However, this method does not fully describe the substantial differences in shape between defects. An alternative method, for example the extreme vertices model [58], may be more applicable for future analysis. The number of defects identified before and after

testing increased in both samples, indicating that the rate of defect growth (possibly from defects below the scan resolution of 10 μm) is greater than the rate of defect coalescence.

In contrast to the complex defects observed via 3D X-ray μCT scanning, those identified via fractography and sectioned sample analysis (Figure 10) generally appear to be spherical. The presence of fatigue striations and ductile dimples on the fracture surface of both cast and forged MarBN are characteristic of fatigue failure in metals (e.g. Figure 10(b, d)). Fatigue striations are generated by repeated crack blunting and sharpening as a result of dislocation slip in the plastic zone at the crack tip and can be used as a measure of the rate of microcrack propagation under constant loading. Ductile dimples on the fracture surface occur due to localised plastic strain due to dislocation accumulation and void growth around defects as a result of decohesion from the matrix. These phenomena have been observed previously on the fracture surface of stainless and martensitic steels [59–61].

Sectioned images of cast and forged MarBN (Figure 10(e – f)) provides further evidence of the role of manufacturing defects in fatigue crack initiation and propagation, with oxide scale formation in cracks and pitting at inclusions. Manufacturing defects have been identified as a primary source of failure; important factors include size, shape, location (i.e. proximity to the gauge length) and distribution [11,62–64]. Oxide scale cracking, due to mechanical loading, promotes diffusion of oxygen along microstructural boundaries, resulting in a weakened matrix material to resist crack initiation and propagation [65]. Furthermore, inclusions are shown to promote oxide pit formation; therefore, the likelihood of crack initiation and propagation in such regions is increased due to both (i) increased stress and strain concentrations and (ii) weakened matrix material. The mechanical properties of inclusions differ from the matrix and there is generally a low-

strength interface bond between inclusions and the matrix. Decohesion or inclusion fracture is found to primarily result from stress concentrations due to dislocation pile-ups at inclusions [4,62,63,66].

The new methodology presented for voxel-based finite element modelling, as per Figure 11, facilitates high quality mesh generation for measured distributions of complex-morphology defects, without the usual problems of poor element quality or element distortion. This method could be readily extended to realistic complex geometries, such as the valve chest geometry presented by O'Hara [40], for example, and new insights may be gained on the influence of complex (measured) manufacturing defects on FCI and related properties of interest.

Significant localised strain is predicted to occur in the region of all defects, particularly due to the increased complexity of defects in the cast sample (Figure 12(a, b)). FCI in the cast material is predicted significantly earlier than the forged (2 cycles versus 23 cycles), due to substantial damage accumulation, with cracking predicted to occur at all casting defects within 100 cycles, highlighting the importance of both defect shape and location.

5. Conclusions

Some key conclusions from this work are as follows:

- A candidate material for next-generation fossil fuel power plant, MarBN, has been characterised with respect to effects of manufacturing-induced defects on high temperature fatigue, via a program of experimental testing, 3D X-ray μCT scanning, microstructural analysis and computational modelling.

- μCT scanning of pre- and post-test specimens indicates (i) the influence of manufacturing process on defect size, shape and distribution, and (ii) the role of defects on fatigue crack initiation and propagation in material failure.
- The complex shape of defects identified in both cast and forged MarBN, in conjunction with factors such as coalescence and location, have been identified as key factors promoting fatigue cracking. Furthermore, the broad range of defect geometries identified (i.e. complex and stringer), including volume fraction and distribution, provide new insight into the effects of manufacturing process (i.e. casting and forging).
- Forged material is shown to have a significantly (approximately 16 times) lower defect volume fraction than cast, with much less geometrical complexity. This contributes to up to 88% increase in high temperature low cycle fatigue life for forged MarBN, when loaded parallel to the forging direction, compared to both cast MarBN and the current generation material, P91 steel.
- A new voxel-based finite element methodology is presented for efficient representation and computational modelling of the three-dimensional effects of complex defect morphologies within a unified viscoplasticity-damage framework, to represent the cyclic evolution and re-distribution of stress-strain-damage localisation.
- The multiaxial, cyclic viscoplasticity model with critical-plane damage corroborates the measured responses and predicts low-cycle fatigue damage initiation at the measured complex defects from very early (typically less than 10 cycles) in the life of the material.

6. Acknowledgements

538 The authors gratefully acknowledge funding from the Irish Research Council and GE
539 Power under the Enterprise Partnership Scheme (EPSPG/2015/55), and the SFI Research
540 Centre for Advanced Manufacturing, I-Form (SFI/16/RC/3872). The authors would like to
541 express their gratitude to those in the IMPEL consortium. The authors acknowledge the
542 facilities and technical assistance of the Centre for Microscopy & Imaging at the National
543 University of Ireland Galway. The authors wish to acknowledge the DJEI/DES/SFI/HEA
544 Irish Centre for High-End Computing (ICHEC) for the provision of computational
545 facilities and support.

References

[1] Parsons Brinckerhoff, Technical Assessment of the Operation of Coal & Gas Fired Plants, (2014) 44.

[2] S.A. Lefton, P.M. Besuner, D.. Agan, The real cost of on/off cycling, Mod. Power Syst. 26 (2006) 11–13.

[3] D. Jandová, J. Kasl, E. Chvostová, Microstructure of CB2 Steel before and after Long-Term Creep Tests, Mater. Sci. Forum. 782 (2014) 311–318. https://doi.org/10.4028/www.scientific.net/MSF.782.311.

[4] F. Abe, M. Tabuchi, H. Semba, M. Igarashi, M. Yoshizawa, N. Komai, A. Fujita, Feasibility of MARBN steel for application to thick section boiler components in USC power plant at 650 C, in: Proc. 5th Int. Conf. Adv. Mater. Technol. Foss. Power Plants, Oct., 2007: pp. 3–5.

[5] T. Hamaguchi, H. Okada, S. Kurihara, H. Hirata, M. Yoshizawa, A. Iseda, MICROSTRUCTURAL EVALUATION OF 9CR-3W-3CO-ND-B HEAT-RESISTANT STEEL (SAVE12AD) AFTER LONG-TERM CREEP DEFORMATION, in: Proc. ASME 2017 Press. Vessel. Pip. Conf., Waikoloa, Hawaii, 2017.

[6] J.P. Shingledecker, N.D. Evans, Creep-rupture performance of 0.07C-23Cr-45Ni-6W-Ti,Nb austenitic alloy (HR6W) tubes, Int. J. Press. Vessel. Pip. 87 (2010) 345–350. https://doi.org/10.1016/j.ijpvp.2010.03.011.

[7] A. Di Gianfrancesco, Materials for ultra-supercritical and advanced ultra-supercritical power plants, 2016. https://doi.org/https://doi.org/10.1016/B978-0-08-100552-1.00001-4.

569 [8] K. Tanaka, T. Mura, A theory of fatigue crack initiation at inclusions, Metall. Trans.
570 A. 13 (1982) 117–123. https://doi.org/10.1007/BF02642422.

571 [9] D. Hull, Fractography: observing, measuring and interpreting fracture surface
572 topography, Cambridge University Press, 1999.

573 [10] D.R. Askeland, P.P. Fulay, W.J. Wright, The science and engineering of materials,
574 2011. https://doi.org/10.2172/15009526.

575 [11] X. Xie, L. Zhang, M. Zhang, J. Dong, K. Bain, Micro-mechanical behavior study of
576 non-metallic inclusions in P/M disk superalloy Rene'95, Superalloys. (2004) 451–
577 458.

578 [12] Q.Y. Wang, C. Bathias, N. Kawagoishi, Q. Chen, Effect of inclusion on subsurface
579 crack initiation and gigacycle fatigue strength, Int. J. Fatigue. 24 (2002) 1269–1274.
580 https://doi.org/10.1016/S0142-1123(02)00037-3.

581 [13] I. Gustavsson, Fatigue limit model for hardened steels, Fatigue Fract. Eng. Mater.
582 Struct. 15 (1992) 881–894.

583 [14] C.P. O'Hagan, B.J. O'Brien, S.B. Leen, R.F.D. Monaghan, A microstructural
584 investigation into the accelerated corrosion of P91 steel during biomass co-firing,
585 Corros. Sci. 3 (2016). https://doi.org/10.1016/j.corsci.2016.03.028.

586 [15] T. Billaudeau, Y. Nadot, G. Bezine, Multiaxial fatigue limit for defective materials :
587 mechanisms and experiments, Acta Mater. 52 (2004) 3911–3920.
588 https://doi.org/10.1016/j.actamat.2004.05.006.

589 [16] R. Prasannavenkatesan, J. Zhang, D.L. McDowell, G.B. Olson, H.J. Jou, 3D
590 modeling of subsurface fatigue crack nucleation potency of primary inclusions in

591 heat treated and shot peened martensitic gear steels, Int. J. Fatigue. 31 (2009) 1176–
592 1189.

593 [17] R.A. Hardin, C. Beckermann, Effect of Porosity on the Stiffness of Cast Steel,
594 Metall. Mater. Trans. A. 38 (2007) 2992–3006. https://doi.org/10.1007/s11661-007-
595 9390-4.

596 [18] L. Babout, E. Maire, R. Foug, Damage initiation in model metallic materials : X-ray
597 tomography and modelling, Acta Mater. 52 (2004) 2475–2487.
598 https://doi.org/10.1016/j.actamat.2004.02.001.

599 [19] X. Wang, X. Li, Q. Li, F. Huang, H. Li, J. Yang, Control of stringer shaped non-
600 metallic inclusions of CaO-Al2O3system in API X80 linepipe steel plates, Steel
601 Res. Int. 85 (2014) 155–163. https://doi.org/10.1002/srin.201300044.

602 [20] A. Mbiakop, A. Constantinescu, K. Danas, European Journal of Mechanics A /
603 Solids On void shape effects of periodic elasto-plastic materials subjected to cyclic
604 loading, Eur. J. Mech. / A Solids. 49 (2015) 481–499.
605 https://doi.org/10.1016/j.euromechsol.2014.09.001.

606 [21] A. Mbiakop, A. Constantinescu, K. Danas, Journal of the Mechanics and Physics of
607 Solids An analytical model for porous single crystals with ellipsoidal voids, J.
608 Mech. Phys. Solids. 84 (2015) 436–467. https://doi.org/10.1016/j.jmps.2015.07.011.

609 [22] R.A. Hardin, C. Beckermann, Prediction of the Fatigue Life of Cast Steel
610 Containing Shrinkage Porosity, Metall. Mater. Trans. A. 40 (2009) 581–597.
611 https://doi.org/10.1007/s11661-008-9755-3.

612 [23] G. Nicoletto, G. Anzelotti, R. Kone, Procedia Engineering X-ray Computed
613 Tomography vs . Metallography for Pore Sizing and Fatigue of Cast Al-alloys,

(2010). https://doi.org/10.1016/j.proeng.2010.03.059.

[24] G. Nicoletto, R. Konec, Characterization of microshrinkage casting defects of Al – Si alloys by X-ray computed tomography and metallography, 41 (2012) 39–46. https://doi.org/10.1016/j.ijfatigue.2012.01.006.

[25] IMPACT - Innovative Materials Design and Monitoring of Power Plant to Accommodate Carbon Capture, (2010). http://gtr.rcuk.ac.uk/projects?ref=100819.

[26] A.A. Saad, Cyclic plasticity and creep of power plant materials, Univ. Nottingham. PhD Thesis (2012).

[27] F. Abe, Precipitate design for creep strengthening of 9% Cr tempered martensitic steel for ultra-supercritical power plants, Sci. Technol. Adv. Mater. 9 (2008) 13002.

[28] L. Li, P. Zhu, G. West, R.C. Thomson, The Effect of Duration of Stress Relief Heat Treatments on Microstructural Evolution and Mechanical Properties in Grade 91 and 92 Power Plant Steels, Adv. Mater. Technol. Foss. Power Plants Proc. from Sixth Int. Conf. 2010 (ASM Int. (2011) 679–692.

[29] The Difference Between Casting & Forging, ATC Gr. (2018).

[30] R.A. Barrett, Experimental Characterisation and Computational Constitutive Modelling of High Temperature Degradation in 9Cr Steels Including Microstructural Effects, PhD Thesis. (2016) National University of Ireland Galway.

[31] R.A. Barrett, E. O'Hara, P.E. O'Donoghue, S.B. Leen, High Temperature Low Cycle Fatigue Behaviour Of MarBN At 600 C, in: ASME 2015 Press. Vessel. Pip. Conf., ASME, 2015: pp. 1–10.

[32] E.M. O'Hara, N.M. Harrison, B.K. Polomski, R.A. Barrett, S.B. Leen, Fatigue

636 damage characterisation of MarBN steel for high temperature flexible operating
637 conditions, Proc. Inst. Mech. Eng. Part L J. Mater. Des. Appl. (2016)
638 1464420716667759. https://doi.org/10.1177/1464420716667759.

639 [33] E.M. O'Hara, N.M. Harrison, B.K. Polomski, R.A. Barrett, S.B. Leen, The effect of
640 inclusions on the high - temperature low - cycle fatigue performance of cast
641 MarBN : Experimental characterisation and computational modelling, Fatigue Fract.
642 Eng. Mater. Struct. 41 (2018) 2288–2304. https://doi.org/10.1111/ffe.12864.

643 [34] J. Heppner, K. Kirsch, Microelectronic Systems: Circuits, Systems and
644 Applications, Springer Science & Business Media, 2011.

645 [35] C.O. Frederick, P.J. Armstrong, A mathematical representation of the multiaxial
646 Bauschinger effect, Mater. High Temp. 24 (2007) 1–26.

647 [36] J.L. Chaboche, G. Rousselier, On the Plastic and Viscoplastic Constitutive
648 Equations—Part I: Rules Developed With Internal Variable Concept, J. Press.
649 Vessel Technol. 105 (1983) 153. https://doi.org/10.1115/1.3264257.

650 [37] J.L. Chaboche, P.M. Lesne, A Non-Linear Continuous Fatigue Damage Model,
651 Fatigue Fract. Eng. Mater. Struct. 11 (1988) 1–17.

652 [38] W.J. Ostergren, A damage foundation hold time and frequency effects in elevated
653 temperature low cycle fatigue, J. Test Eval. (1967) 327–339.

654 [39] T.P. Farragher, S. Scully, N.P. O'Dowd, S.B. Leen, Development of life assessment
655 procedures for power plant headers operated under flexible loading scenarios, Int. J.
656 Fatigue. 49 (2013) 50–61.

657 [40] E. O'Hara, An experimental and computational investigation of the high

temperature behaviour of MarBN steel with application to effects of manufacturing, PhD Thesis. (2018) National University of Ireland Galway.

[41] D.M. Grogan, S.B. Leen, C.O.A. Semprimoschnig, C.M.Ó. Brádaigh, Composites : Part A Damage characterisation of cryogenically cycled carbon fibre / PEEK laminates, Compos. Part A. 66 (2014) 237–250. https://doi.org/10.1016/j.compositesa.2014.08.007.

[42] C. Gupta, H. Toda, C. Schlacher, Y. Adachi, P. Mayr, C. Sommitsch, K. Uesugi, Y. Suzuki, A. Takeuchi, M. Kobayashi, Study of creep cavitation behavior in tempered martensitic steel using synchrotron micro-tomography and serial sectioning techniques, Mater. Sci. Eng. A. 564 (2013) 525–538. https://doi.org/10.1016/j.msea.2012.12.002.

[43] R.A. Barrett, P.E. O'Donoghue, S.B. Leen, A physically-based high temperature yield strength model for 9Cr steels, Mater. Sci. Eng. A. 730 (2018) 410–424. https://doi.org/10.1016/j.msea.2018.05.086.

[44] B. Fournier, F. Dalle, M. Sauzay, J. Longour, M. Salvi, C. Caes, I. Tournie, P.F. Giroux, S.H. Kim, Comparison of various 9-12%Cr steels under fatigue and creep-fatigue loadings at high temperature, Mater. Sci. Eng. A. 528 (2011) 6934–6945. https://doi.org/10.1016/j.msea.2011.05.046.

[45] S. Mrozin, Low cycle fatigue and cyclic softening behaviour of martensitic cast steel, 35 (2013) 692–702. https://doi.org/10.1016/j.engfailanal.2013.06.019.

[46] R.A. Barrett, P.E. O'Donoghue, S.B. Leen, A dislocation-based model for high temperature cyclic viscoplasticity of 9–12Cr steels, Comput. Mater. Sci. 92 (2014) 286–297.

681 [47] H. Semba, F. Abe, Alloy design and creep strength of advanced 9% Cr USC Boiler
682 steels containing high concentration of boron, Energy Mater. 1. (2006) 238–244.

683 [48] K. Sakuraya, H. Okada, F. Abe, BN type inclusions formed in high Cr ferritic heat
684 resistant steel, Energy Mater. 1 (2006) 158–166.

685 [49] K. Maruyama, K. Sawada, J. Koike, Strengthening mechanisms of creep resistant
686 tempered martensitic steel, ISIJ Int. 41 (2001) 641–653.

687 [50] X. Wang, Q. Xu, S.M. Yu, L. Hu, H. Liu, Y.Y. Ren, Laves-phase evolution during
688 aging in 9Cr-1.8W-0.5Mo-VNb steel for USC power plants, Mater. Chem. Phys.
689 163 (2015) 219–228. https://doi.org/10.1016/j.matchemphys.2015.07.032.

690 [51] J. Hald, Microstructure and long-term creep properties of 9-12% Cr steels, Int. J.
691 Press. Vessel. Pip. 85 (2008) 30–37. https://doi.org/10.1016/j.ijpvp.2007.06.010.

692 [52] G. Golański, C. Kolan, J. Jasak, Degradation of the Microstructure and Mechanical
693 Properties of High-Chromium Steels Used in the Power Industry, Creep. (2018).
694 https://doi.org/10.5772/intechopen.70552.

695 [53] E. Pessard, F. Morel, A. Morel, D. Bellett, Modelling the role of non-metallic
696 inclusions on the anisotropic fatigue behaviour of forged steel, Int. J. Fatigue. 33
697 (2011) 568–577. https://doi.org/10.1016/j.ijfatigue.2010.10.012.

698 [54] L. Salvo, P. Cloetens, E. Maire, S. Zabler, J.J. Blandin, W. Ludwig, E. Boller, D.
699 Bellet, C. Josserond, X-ray micro-tomography an attractive characterisation
700 technique in materials science, 200 (2003) 273–286.

701 [55] A. Isaac, F. Sket, W. Reimers, B. Camin, G. Sauthoff, A.R. Pyzalla, In situ 3D
702 quantification of the evolution of creep cavity size, shape, and spatial orientation

using synchrotron X-ray tomography, Mater. Sci. Eng. A. 478 (2008) 108–118. https://doi.org/10.1016/j.msea.2007.05.108.

[56] A. Isaac, K. Dzieciol, F. Sket, A. Borbély, In-situ microtomographic characterization of single-cavity growth during high-temperature creep of leaded brass, Metall. Mater. Trans. A Phys. Metall. Mater. Sci. 42 (2011) 3022–3030. https://doi.org/10.1007/s11661-011-0781-1.

[57] J.C. Earthman, G. Eggeler, B. Ilschner, Deformation and damage processes in a 12%CrMoV steel under high temperature low cycle fatigue conditions in air and vacuum, Mater. Sci. Eng. A. 110 (1989) 103–114. https://doi.org/10.1016/0921-5093(89)90161-5.

[58] I. Cruz-Matías, D. Ayala, D. Hiller, S. Gutsch, M. Zacharias, S. Estradé, F. Peiró, Sphericity and roundness computation for particles using the extreme vertices model, J. Comput. Sci. 30 (2019) 28–40. https://doi.org/10.1016/j.jocs.2018.11.005.

[59] B. Xiao, L. Xu, L. Zhao, H. Jing, Y. Han, Tensile mechanical properties, constitutive equations, and fracture mechanisms of a novel 9% chromium tempered martensitic steel at elevated temperatures, Mater. Sci. Eng. A. 690 (2017) 104–119. https://doi.org/10.1016/j.msea.2017.02.099.

[60] B. Xiao, L. Xu, L. Zhao, H. Jing, Y. Han, Y. Zhang, Creep properties, creep deformation behavior, and microstructural evolution of 9Cr-3W-3Co-1CuVNbB martensite ferritic steel, Mater. Sci. Eng. A. 711 (2018) 434–447. https://doi.org/10.1016/j.msea.2017.11.061.

[61] J. Lu, FINITE ELEMENT MODELLING OF THE CYCLIC PLASTICITY BEHAVIOUR OF This Thesis is Dedicated to Menghao Chen and, (2015).

[62] F. Ellyin, Fatigue damage, crack growth and life prediction, Springer Science & Business Media, 2012.

[63] S. Murakami, Continuum damage mechanics: a continuum mechanics approach to the analysis of damage and fracture, Springer Science & Business Media, 2012.

[64] F.C. Campbell, Fatigue and Fracture: Understanding the Basics, 2012. https://doi.org/10.1017/CBO9781107415324.004.

[65] B. Fournier, M. Sauzay, C. Caës, M. Noblecourt, M. Mottot, A. Bougault, V. Rabeau, A. Pineau, Creep-fatigue-oxidation interactions in a 9Cr-1Mo martensitic steel. Part I: Effect of tensile holding period on fatigue lifetime, Int. J. Fatigue. 30 (2008) 649–662. https://doi.org/10.1016/j.ijfatigue.2007.05.007.

[66] J.-L. Chaboche, G. Rousselier, On the plastic and viscoplastic constitutive equations—Part II: application of internal variable concepts to the 316 stainless steel, J. Press. Vessel Technol. 105 (1983) 159–164.